

Understanding the nanoscale structure of hexagonal phase lyotropic liquid crystal membranes

Benjamin J. Coscia Douglas L. Gin Richard D. Noble Joe Yelk

Matthew Glaser Xunda Feng Michael R. Shirts

December 15, 2017

1 Introduction

Nanostructured membrane materials have become increasingly popular for aqueous separations applications such as desalination and biorefinement because they offer the ability to control membrane architecture at the atomic scale permitting the design of solute-specific separation membranes. [1] Most membrane-based aqueous separations of small molecules can be achieved using reverse osmosis (RO) or nanofiltration (NF) [2]. While RO and NF have seen many advances in the past few decades, they are far from perfect separation technologies.

Current commercial RO membranes are thin film composite membranes with a porous support layer and an active layer made of a dense polymer matrix. The membranes are unstructured with tortuous and polydisperse diffusion pathways. Separation occurs based on differences in solubility and diffusivity of solutes within the polymer matrix [3]. With optimization, one can exploit these differences to create a functional selective barrier. RO operation costs are suboptimal because high feed pressures are required in order to achieve a useful solvent flux.

Improved RO membranes can make desalination more sustainable. Only 0.5 % of the world's water is fresh. Desalination is an important source of potable water, necessary in order to keep up with demand generated by a rapidly growing global population. Although RO is currently the cheapest form of desalination, the cost must be further decreased in order to meet demand. A typical seawater desalination process requires feed pressures in the range of 800 to 1000 psi [4]. By designing better membranes for desalination, we can achieve higher water fluxes and reduce feed pressure requirements which will decrease the cost of fresh water production. [1].

NF was introduced as an intermediate between RO and ultrafiltration, having the ability to separate organic matter and salts on the order of one nanometer in size. Explicit pore pathways running through the thickness of the membrane permit high solvent fluxes at lower pressures than RO. NF membranes typically have a surface charge resulting from ionizable groups which affords separation of ions smaller than the pore radius by the mechanism of Donnan exclusion [2]. NF is often used as a precursor to reverse osmosis since it can efficiently remove a significant portion of dissolved solutes. Following NF pretreatment, RO can further purify the permeate. Unfortunately, NF membranes, like RO, possess a pore size distribution which limits their ability to perform precise separations [5]. An NF membrane with high selectivity could offer the versatility to separate ions as well as small charged and uncharged molecules to the same degree as RO and at a significantly lower cost.

Nanostructured membranes can bypass many of the performance issues which plague traditional NF and RO membranes. One can accomplish targeted separations with high selectivity by tuning shape, size and functionality of the molecular building blocks which form these materials. As a result, solute rejecting pores can have their sizes tuned uniformly, resulting in strict size cut-offs. Entirely different mechanisms may govern transport in a given nanostructured material which can inspire novel separation techniques.

Development of nanostructured materials has been limited by the ability to synthesize and scale various fundamentally sound technologies. Graphene sheets are atomically thick which results in excellent water permeability but defects during manufacturing severely impact selectivity [6]. Molecular dynamics (MD) simulations of carbon nanotubes show promise [1] but synthetic techniques are unable to achieve scalable alignment and pore monodispersity. [7, 8] Zeolites have sub-nm pores with a narrow pore size distribution and MD simulations exhibit complete rejection of solvated ions, [9] however, experimental rejection was low and attributed to interstitial defects formed during membrane synthesis. [10] There is a need for a scalable nanostructured membrane.

Self assembling lyotropic liquid crystals (LLCs) are a suitable candidate for aqueous separation applications. LLCs share the characteristic ability of nanostructured membrane materials to create highly ordered structures with the added benefits of low cost and synthetic techniques feasible for large scale production. [11] LLC systems created by the monomer Na-GA3C11 (Fig. 1a) have been extensively studied experimentally. [12, 13, 14, 11, 15] Neat liquid crystal monomer forms the thermotropic, Col_h phase (Fig.1). The presence of ca. 10 wt % water results in the H_{II} phase. In both cases, monomers assemble into mesophases made of hexagonally packed, uniform size, cylinders with hydrophilic head groups oriented inward towards the cylinder center. The hydrophilic region can act as a pore for aqueous separations. One can envision tailoring the pore region for specific separations by changing the monomer chemsity.

Research into LLC membranes has been revived in recent years. During early stages of exploration,

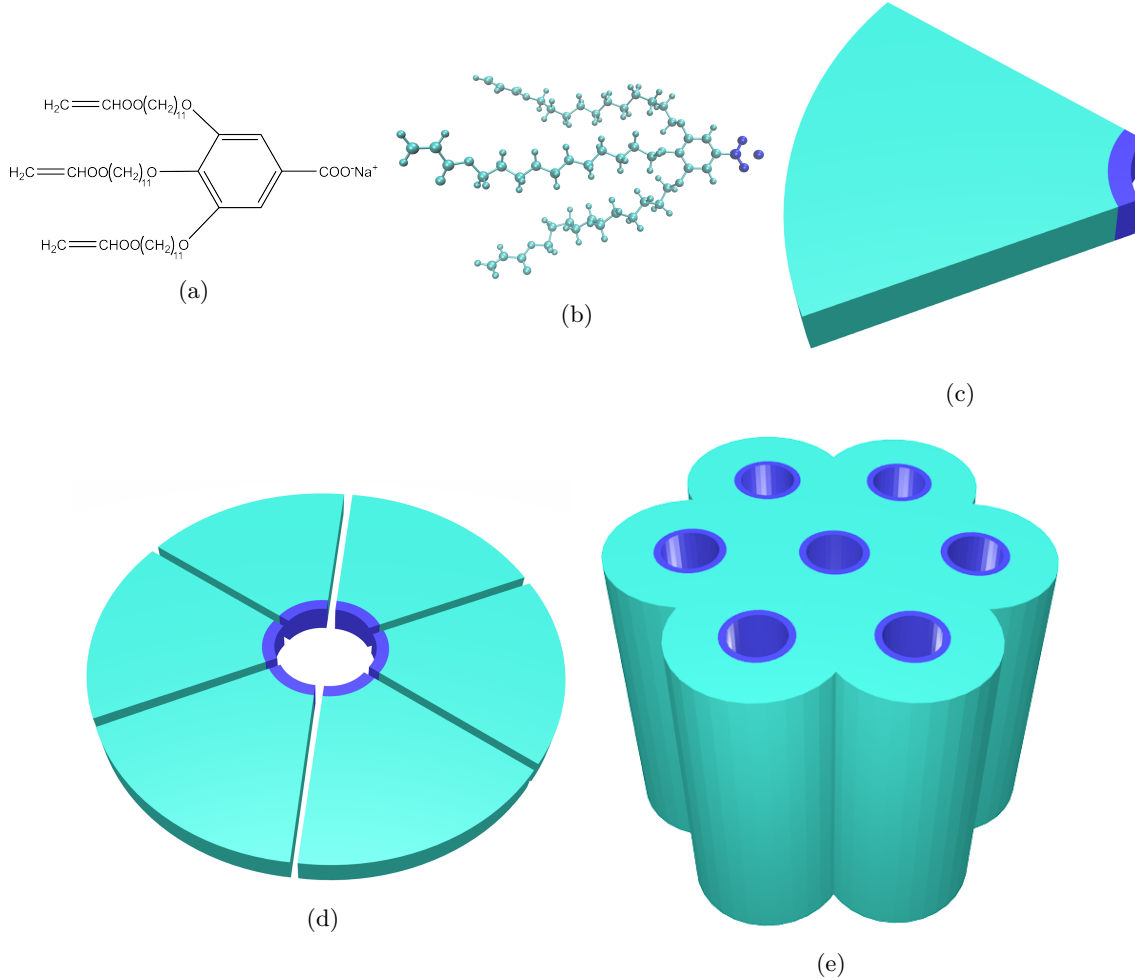


Figure 1: The liquid crystal monomer Na-GA3C11 (a) rendered atomistically (b) exhibits wedge-like character (c). Monomer wedges assemble into disks (d) with hydrophilic head groups (blue) facing towards the disk center. The disks assemble into hexagonally packed columnar mesophases (e)

mesophases formed by Na-GA3C11 could not be macroscopically aligned, resulting in low flux membranes, and no clear route towards scalable and economical filtration. In 2014, Feng et al. showed that the mesophases could be aligned using a magnetic field with subsequent crosslinking to lock the structure in place [11]. In 2016, Feng et al. showed that the same result could be obtained using a technique termed soft confinement [15].

Our current understanding of LLC systems is not rich enough to be able to precisely design membranes for specific separations. Over the past 20 years, H_{II} phase LLC membrane studies have been limited primarily to Na-GA3C11 with some characterization done after minor structural modifications. Resel et al. varied the length of the monomer tails and the counterion used and observed its affect on pore spacing [16]. Their study offers no insight into dynamics within the pore. In a later study of rejection performance, it was

shown that membranes formed by Na-GA3C11 can not perform separations of solutes less than 1.2 nm in diameter because the pores are too large [13]. We do not yet understand how to controllably reduce the effective pore size or how to tune the chemical environment in the nanopores for effective water desalination and small organic molecule separations. The only source of predictive modeling for LLC systems have been macroscopic models which likely do not adequately describe transport at these length scales [17]. It will be challenging to efficiently narrow down the large design space in a laboratory setting without a robust model.

A molecular level understanding of LLC membrane structure, enabled by molecular dynamics simulations, will provide guidelines to reduce the large chemical space available to design monomers for creation of separation-specific membranes. A good molecular model should incorporate a detailed picture of the nanoscopic pore structure which will be crucial to understanding the role of monomer structure in solute transport and membrane design. Models resulting from molecular dynamics simulations will provide the required level of detail (Fig. 2). We can directly observe solute transport and suggest governing mechanisms. We can observe how the choice of head group may influence pore size for size exclusion driven separations. We can interchange counterions which may influence both the pore size and the strength of the Donnan potential which affects the degree to which the membrane can exclude charged species.

In order to appropriately model transport, we must first gain a thorough understanding of the nanoscopic structure of LLC membranes. Our approach to constructing a general model will follow the development of a model of the assembly formed by Na-GA3C11 since it has sufficient experimental characterization. We have also narrowed our scope to the development of a model of the Col_h phase membrane. Compared to the H_{II} phase, the Col_h phase is a simpler starting point, due to the absence of water, and has detailed experimental wide-angle X-ray scattering (WAXS) patterns useful for reconstructing structural data.

Despite having structural data, there is still information which experiment cannot definitively answer. There are several key questions that we will investigate.

Monomers in the Col_h system are theorized to be partitioned into stacked layers which form columnar pores. We want to know

1. If layers do exist, how many monomers constitute a single layer?

A simple molecular simulation study of a similar molecule suggested that there are 4 monomers in each layer. Their estimation is based on a simulated system containing only 16 total monomers which likely does not sufficiently model the chemical environment present in the real system [18]. A separate calculation based on the volume of the liquid crystal monomers proposes that there are seven monomers in each layer [16]. A molecular model orders of magnitude larger than any other reported atomistic liquid crystal membrane simulations has the best chance of directly answering this question. We will

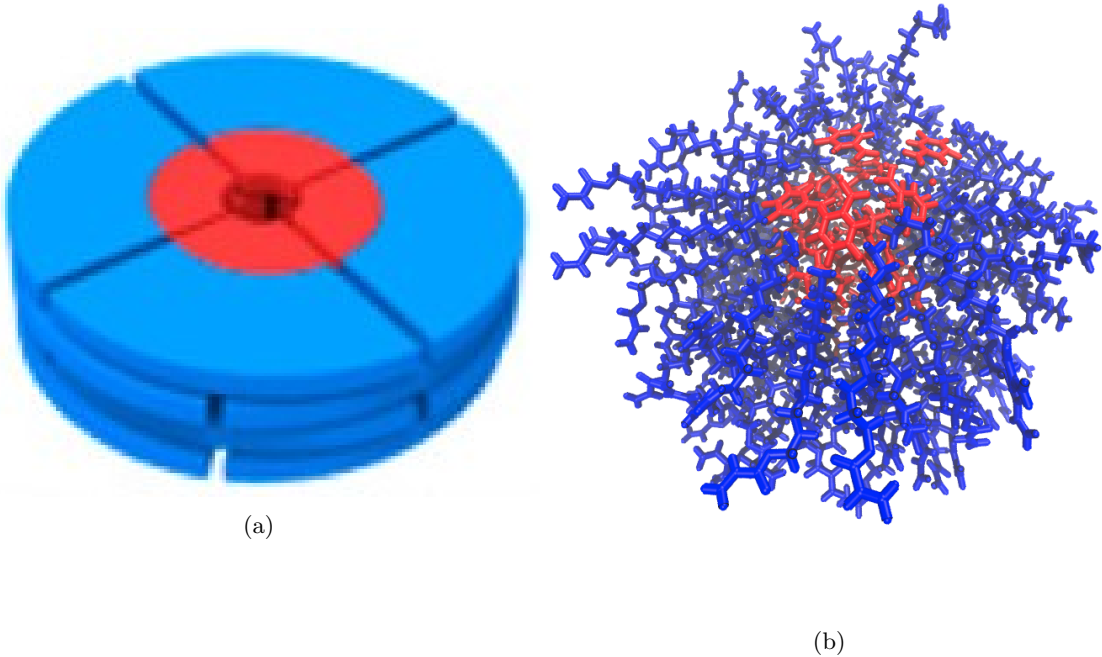


Figure 2: (a) Our previous understanding of the pore structure allows us to speculate about separation behavior. (b) A detailed molecular model will allow us to directly observe solute transport. Here, four stacked layers of 5 monomers are pictured atomistically. The hydrophilic region is in red and the hydrophobic region is colored blue.

directly change the layer composition and note its effect on membrane structure.

2. Does our model support the existence of layers and if so, how well defined are the layers?

Experimentally, their existence is supported by evidence of strong π - π stacking interactions in the direction perpendicular to the membrane plane. π - π stacking will only occur between the aromatic monomer head groups which leaves no description of what is happening in the monomer tail region. The tails may entangle isotropically while stacking order is maintained among headgroups.

3. How do monomers in each layer position themselves with respect to surrounding layers?

The π - π stacking interactions may be a driving force of self assembly in this system [19]. Gas phase ab initio studies of benzene dimers have shown a clear energetic advantage for parallel displaced and T-shaped π - π stacking conformations versus a sandwiched conformation [20]. Substituted benzene rings exhibit an even stronger π - π stacking attraction which favors the parallel displaced configuration in all cases except where the substitutions are extremely electron withdrawing. [21, 22]. We will compare simulated X-ray diffraction patterns to experiment in order to deduce which stacking configurations is most likely.

4. Can the system exist in other metastable states or phases that are not accessed during experiments?

There remains the possibility that there is more than one metastable state associated with a given LLC system. Simulating a membrane atomistically will require many atoms which limits the timescales accessible with MD. It is reasonable to expect that we will generate configurations which are kinetically trapped in a metastable free energy basin. We must be able to identify which state is produced experimentally.

5. What constitutes a pore and how well-defined are the pore regions?

The limited picture that experiment provides tells us that there are hexagonally packed, hydrophilic regions where transport is likely to occur. One may instinctively assume that these regions are tube-like pathways. We will explore the composition of the pores and the partition between the hydrophilic and hydrophobic regions.

6. Is it necessary to include any water in order to appropriately model the Col_h phase?

While the Col_h phase is described as dry, it has been suggested by experimentalists, in unpublished communications, that it is likely that small amounts of ambient water are leached into neat monomer. Experimentally, achieving a hexagonal phase with a completely dry system has proven difficult. If neat monomer is allowed to sit in ambient conditions, its color turns from transparent to slightly opaque and

a hexagonal phase forms. Although we will not explore whether water is necessary for self assembly, we hypothesize that the hydrogen bonding network formed by the water may play a role in structuring the pores and holding together the hexagonal phase. We can use simulated X-ray diffraction patterns to see if there is any meaningful structural difference between a "dry" and "wet" system.

We used experimental small-angle X-ray scattering (SAXS) data from [15] (Fig. 3a) and wide angle X-ray scattering (WAXS) data (Fig. 3b, produced as described in [11]) for comparison to our model. We rely primarily on the 2D WAXS data since it encodes all structural details down to the sub-nm scale. There are five major features of interest present in the 2D experimental pattern shown in Figure 3b. The first is located at $q_z = 1.7 \text{ \AA}^{-1}$, corresponding to a real space separation of 3.7 \AA . The reflection is attributed to π - π stacking between aromatic rings in the direction perpendicular to the membrane plane, or z-axis [11]. For simplicity, this reflection will be referred to as R- π . A weak intensity line is located at exactly half the q_z value of R- π ($q_z = 0.85 \text{ \AA}^{-1}$), corresponding to a real space periodic spacing of 7.4 \AA . This reflection has been interpreted as 2_1 helical ordering of aromatic rings along the z axis meaning if the positions of the aromatic rings can be traced by a helix, then for each full turn in the helix, one will encounter two aromatic rings. For this reason it will be referred to as R-helix. A third major reflection is marked by a low intensity ring located at $r = 1.4 \text{ \AA}^{-1}$. The real space separation corresponds to 4.5 \AA which is characteristic of the average spacing between packed alkane chains. This reflection will be called R-alkanes. Within R-alkanes, are four spots of higher relative intensity which will be called R-spots. All are located ≈ 37 degrees from the q_z axis in their respective quadrants. In many liquid crystal systems this can be explained by the tilt angle of the alkane chains with respect to the membrane plane. The final feature corresponds to the spacing and symmetry of the d_{100} plane which can be related to the distance between pores. The feature, which will be called R-pores, is characterized by dots along $q_z = 0$. The spacing between dots is indicative of the hexagonal symmetry of the packed pores. The same information at higher resolution is obtained using a SAXS setup.

In this study, we build a significantly more realistic atomistic model of LLC membranes than, to our knowledge, has ever previously been done, and explore what new structural information can be gained and what structure hypotheses are supported by this model. We validate the model using as much experimental information as possible. We are most interested in reproducing the conclusions about structure which have been drawn from X-ray diffraction (XRD) experiments and in matching ionic conductivity measurements [15].

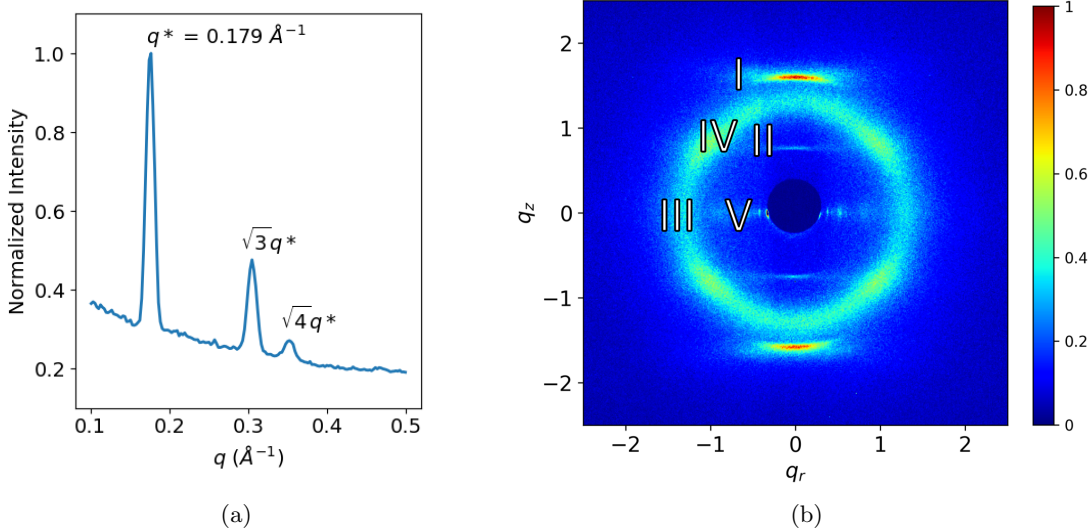


Figure 3: (a) The repeat spacing in the 1D small angle X-ray scattering pattern is characteristic of hexagonal packing. The leading peak represents the distance between the d_{100} planes. Using this distance, we know that the distance between pore centers is 4.12 nm. (b) 2D wide angle X-ray scattering gives details about repeating features less than 1 nanometer apart. Experimentalists have justified each of the 5 major reflections present as follows: (I) Aromatic head group $\pi - \pi$ stack 3.7 \AA apart. (II) Monomers arrange vertically in a 2_1 helix. (III) Alkane chain tails pack 4.5 \AA apart. (IV) Monomer tails tilt with respect to the membrane plane. (V) As derived from SAXS, pores pack hexagonally and are spaced 4.12 nm apart

2 Methods

2.1 Monomer Parameterization

Liquid crystal monomers were parameterized using the Generalized AMBER Forcefield [23] with the Antechamber package [24] provided with AmberTools16 [25]. Atomic charges were assigned using the am1bccsym method of molcharge shipped with QUACPAC from Openeye Scientific Software. All molecular dynamics simulations were run using Gromacs 2016. [26, 27, 28, 29]

An ensemble of characteristic, low-energy vacuum monomer configurations were constructed by applying a simulated annealing process to a parameterized monomer. Monomers were cooled from 1000K to 50K over 10 nanoseconds. A low energy configuration was randomly pulled from the trajectory and charges were reassigned using molcharge. Using the new charges, the monomer system was annealed again and a random monomer configuration was pulled from the trajectory to be used for full system construction (Figure 4a).

2.2 Unit Cell Preparation

The timescale for self assembly of monomers into the hexagonal phase is unknown and likely outside of a reasonable length for an atomistic simulation, calling for a more efficient way to build the system. Previous

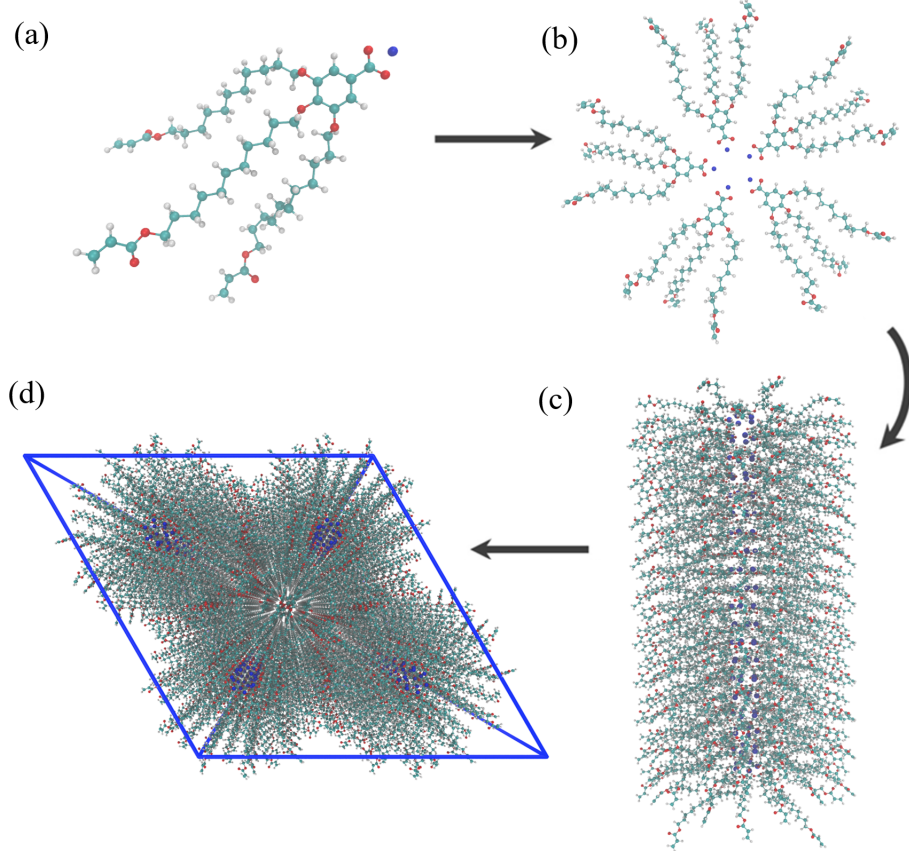


Figure 4: (a) A single monomer was parameterized and annealed to produce a low energy configuration. (b) Monomers are rotated and assembled into layers with hydrophobic centers. (c) Twenty layers are stacked on top of each other to create a pore. (d) Pores are duplicated and placed into a monoclinic unit cell

work has shown a coarse grain model self assemble into the H_{II} phase configuration in ≈ 1000 ns [30]. We attempted atomistic self-assembly by packing monomers into a box using Packmol [31]. Simulations of greater than 100 ns show no indicators of progress towards an ordered system To bypass the slow self-assembly process, python scripts are used to assemble monomers into a structure close to one of a number of hypothesized equilibrium configurations (Figure 4).

A typical simulation volume contains four pores in a monoclinic unit cell, the smallest unit cell that maintains hexagonal symmetry when extended periodically. Each pore is made of twenty stacked monomer layers with periodic continuity in the z direction, avoiding any edge effects and creating an infinite length pore ideal for studying transport. A small number of layers is preferred in order to reduce computational cost and to allow us to look at longer timescales. Ultimately, we chose to build a system with 20 monomer layers in each pore in order to obtain sufficient resolution when simulating X-ray diffraction patterns.

2.3 Monomer Placement

When constructing an initial configuration, there are a number of variables which require careful consideration while placing monomers. The equilibrium configuration is sensitive to some while insensitive to others. The starting pore radius, defined as the distance of a chosen head group carbon from the pore's central axis, does not influence the equilibrium structure when a reasonable value is chosen (See Supplemental). The pore radius is chosen to be 0.6 nm in our initial configurations because the pore size is estimated to be \approx 1.2 nm. The initial distance between pores also has little effect on the the equilibrated structure. However, one should not start them too close or there will be high energy repulsions during early equilibration. We chose an initial pore spacing of 4.5 nm, \approx 10 % larger than the experimental value of 4.12 nm. The distance between layers, the rotation of the layers with respect to adjacent layers, and the number of monomers per layer do influence the equilibrium structure and require further justification for their choices. We rely on experimental data to inform them.

We chose the layer spacing for the initial configuration based on R- π and then allowed the system to readjust during equilibration. Each monomer was rotated so the plane of the aromatic head groups would be coplanar with the xy plane. We explore two different initial layer spacings. The first is exactly equal to R- π with layers placed so aromatic rings are stacked 3.7 Å apart in the z-direction. A second system is explored with an initial layer spacing of 5 Å. A third system with an initial layer spacing of 10 Å was briefly explored. When layers are spaced out too far, they will collapse on each other while simultaneously slipping in between layers of adjacent pores which leads to an artificially thick membrane with pores spaced closely together. There will be no further discussion of this system but the interested reader can learn more about it in the supplemental information.

The relative interlayer orientation was chosen based on clues from diffraction data as well as the various known stacking modes of benzene and substituted benzene rings: sandwiched, parallel-displaced and T-shaped [20] (Figures 5a to 5c). The T-shaped configuration was ruled out because its \approx 5 Å equilibrium stacking distance [20] is inconsistent with R- π . It is also unfeasible for the monomers to orient in the T-shaped conformation because of the bulky tail groups. The system's preference towards the sandwiched vs. parallel displaced stacking modes will be explored in some detail. Both have reported stacking distances near the R- π value of 3.7 Å. Headgroups in our sandwiched initial configuration are stacked directly on top of each other while stacked headgroups in the parallel displaced initial configuration are offset by $180/n_{mon}$ degrees where n_{mon} equals the number of monomers per layer.

As outlined in (1) the number of monomers in each layer is unknown. We tested configurations constructed with a varied number of monomers per layer. Systems were built in the offset and parallel displaced

configurations with 4, 5, 6, 7 and 8 monomers per layer.

2.4 Equilibration

We developed equilibration schemes to create dry and wet configurations. Both schemes start with an initial configuration generated according to the previous guidelines. To create a dry configuration, we fix monomer head groups in the sandwiched or parallel-displaced configuration using position restraints with a force constant of $1\text{e}6 \text{ KJ mol}^{-1} \text{ nm}^{-2}$. We run a 50 ps simulation in the NVT ensemble which allows the monomer tails to settle without disrupting the ordering of the head groups. Doing so also mitigates system dependence on initial monomer configuration. Every 50 ps, we reduce the force constants by the square root of its previous value. Once the force constant is below $10 \text{ KJ mol}^{-1} \text{ nm}^{-2}$, the restraints are released linearly until there is no more restraining potential. The resulting unrestrained structure is allowed to equilibrate for 5 ns in the NPT ensemble with pressure controlled by the berendsen barostat. Next, we run long NPT equilibration simulations for at least 400 ns using the Parrinello-Rahman barostat with a time constant of 10 ps.

In order to create a wet system, we solvated an initial configuration with water using gmx solvate. All water molecules placed outside the pore region are removed. Waters inside the pore region are randomly removed until the desired concentration of water in the pores is reached. The remainder of the equilibration follows the same procedure as the dry system.

2.5 Crosslinking

In order to fully match synthetic procedures, we created a crosslinking algorithm that can be applied to equilibrated structures. The purpose of crosslinking is to maintain macroscopic alignment of the crystalline domains, ensuring aligned, hexagonally packed pores. For that reason, we are not concerned with replicating the kinetics of the reaction, but instead emphasize the consistency of the final structure with experimental structural data. The algorithm was developed based on the known reaction mechanism. Crosslinking of this system is a free radical polymerization (FRP) taking place between terminal vinyl groups present on each of the three monomer tails. FRPs require an initiator which bonds to the system, meaning new atoms are introduced into the system. For simplicity, the initiator was simulated as hydrogen and made present in the simulation by including them in all possible locations where an addition could occur as dummy atoms. The crosslinking procedure is carried out iteratively. During each iteration, bonding carbon atoms are chosen based on a distance cut-off. The topology is updated with new bonds and dummy hydrogen atoms are changed to appropriate hydrogen types. Head-to-tail addition was the only propagation mode considered

due to its dominance in the real system. Direction of attack was not considered because the resultant mixture is racemic.

Our implementation requires long simulation times to achieve high degrees of crosslinking. For that reason we did not crosslink all systems tested, but only the most promising structure. We show that crosslinking does not significantly change any of our drawn conclusions in Section 3.6.

2.6 Equilibrium Calculations

Using equilibrated structures, we carry out various calculations to characterize the system. We define the point at which a system is equilibrated based on when the distance between pores stops changing.

To calculate the equilibrated pore spacing, we measured the distance between pore centers. Pore centers are located by averaging the coordinates of sodium ions in their respective pores. Pore spacing statistics were generated using the bootstrapping technique (See Supplemental Information).

To quantify the degree of layering and the equilibrium distance between layers in our system, we calculate a spatial correlation function, $g(z)$, measured along the z-axis (perpendicular to the membrane plane). To calculate $g(z)$, we binned the z-component distances between the center of mass of each component and all others of the same pore over at least 50 ns of equilibrated trajectory and then normalized by the average number density. To extract the average distance between layers we applied a discrete fourier transform to $g(z)$ and extracted the highest intensity frequency.

Simulated X-ray diffraction patterns are generated based on atomic coordinates in order to make a direct experimental comparison. All atomic coordinates were simulated as gaussian spheres of electron density corresponding to each atom's atomic number. A three dimensional fourier transform (FT) of the array of electron density results in a three dimensional structure factor which represents the unit cell in reciprocal space. We matched experimental 2D WAXS patterns by adjusting the initial spacing between layers and the orientation of the head groups with respect to adjacent layers.

The colorbars on all diffraction patterns are normalized relative to R-alkanes. We calculated the average intensity within R-alkanes of the experimental pattern, I_{avg} . We exclude intensities within $\pm 30^\circ$ of the $q_r = 0$ axis, since the simulated patterns differ from experiment in those regions (See Fig. 8). We multiplied I_{avg} by a scaling factor of 2.5. Intensities that appear in the experimental pattern $\geq 2.5*I_{avg}$ receive colorbar values of 1. The result of this colorbar scaling method is shown in Figure 3b. We apply the same scaling method to the simulated patterns.

We explored the pore composition by measuring the average number densities of various monomer components as a function of distance from the pore centers. We looked at the average number density of sodium

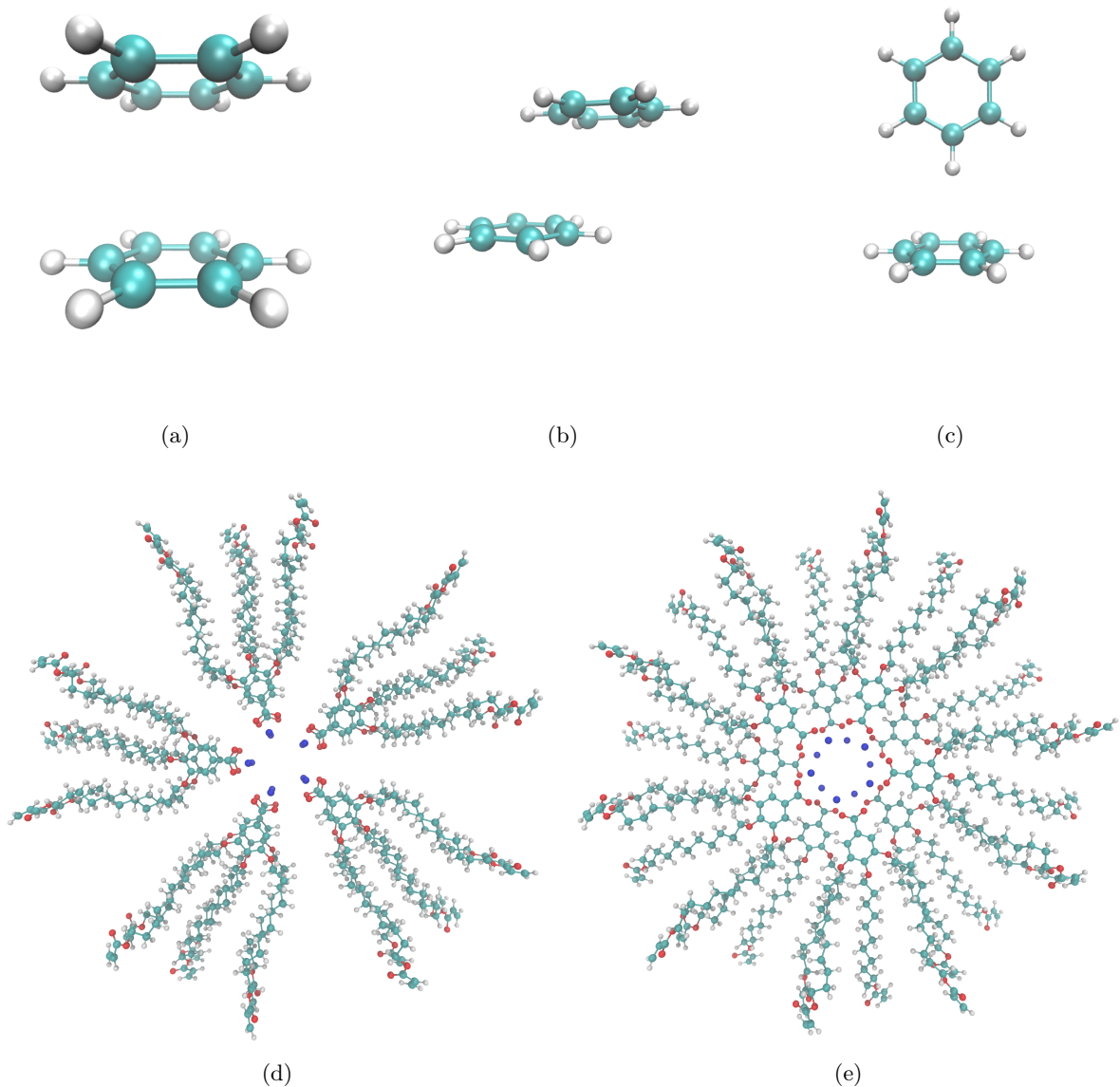


Figure 5: (a) Sandwiched benzene dimers stack 3.8 Å apart. (b) Parallel-Displaced benzene dimers stack 3.4 Å vertically and 1.6 Å horizontally apart. (c) T-shaped benzene dimers stack 5.0 Å apart. (d) Two monomer layers stacked in the sandwiched configuration (e) Two monomer layers stacked in the parallel-displaced configuration

ions, aromatic rings and carbon atoms making up the monomer tails. The radial distance of all atoms in each group from the pore centers are binned, then normalized by the volume of the annulus defined by the bin edges and z box vector.

We calculated ionic conductivity using two different methods for robustness. The Nernst-Einstein relation relates the DC ionic conductivity to ion diffusivity, D , concentration, C , ion charge, q , the boltzmann constant, k_b , and temperature, T :

$$\sigma = \frac{q^2 C D}{k_b T}$$

Sodium ion diffusion coefficients were found by calculating the slope of the linear region of the z-direction mean square displacement curve as indicated by the einstein relation [32]. We visualized the MSD plot to determine where to begin and end a linear fit. Ion concentration was measured with respect to the volume of the entire unit cell.

The second method, termed the Collective Diffusion model, measures the movement of the collective variable, Q , which is defined as the amount of charge transfer through the system and can be thought to represent the center of charge of the system. The conductance, γ of the system can be calculated as:

$$\gamma = \frac{D_Q}{k_b T}$$

Conversion to ionic conductivity is achieved by multiplying by channel length and dividing by the membrane cross sectional area. D_Q is the diffusion coefficient of the collective variable Q . It can be calculated using the einstein relation. A full derivation of the model can be accessed elsewhere [33].

3 Results and Discussion

3.1 Determining the Spatial Configuration of Monomers

Our simulations best support a model built with 5 monomers per layer based on the measured equilibrated pore-to-pore distances. To discern the composition of the monomer layers, addressing (1), we ran simulations of systems created with 4 - 8 monomers per layer. Systems were built in both the parallel displaced and sandwiched configurations with layers initially spaced 3.7 Å apart. Equilibrated configurations were prepared according to the dry equilibration procedure. All systems are stable after 400 ns of simulation. In a sense, all systems are at least metastable, addressing (4), however not all will make physical sense or fit the experimental profile that we are looking to match. Figure 6 shows the pore spacing for all systems tested. Systems built with 5 monomers in each layer equilibrate to a pore spacing that is most consistent with

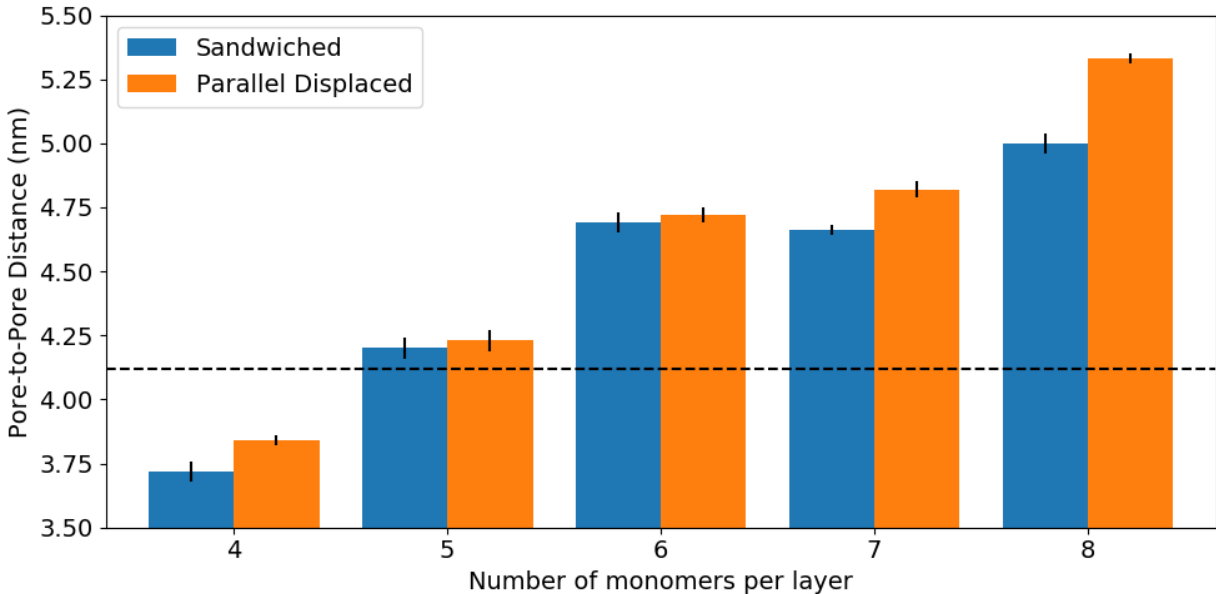


Figure 6: Systems built with 5 monomers per layer in a parallel displaced configuration result in a pore spacing closest to the experimental value of 4.12 nm. The pore spacing of the model increases as number of monomers in each layer increases. The pore spacing of a system starting in the sandwiched configuration is systematically lower than that started in an offset configuration.

the experimental value of 4.12 nm derived from SAXS measurements (Figure 3a). The remainder of this discussion will focus on the analysis of systems built with 5 monomers per layer.

We learned that layers are well-defined and persistent, answering (2). We established our conclusion by plotting the pair correlation function, $g(z)$, calculated between atoms along the length of the pores (Fig. 7). We measured $g(z)$ with respect to aromatic rings in the head groups and, separately, with respect to carbon atoms in the alkane chains. Using a fourier transform of $g(z)$, we see that sandwiched configuration layers stack 4.39 Å apart while parallel displaced configuration layers stack 4.38 Å apart.

We answer question (3) by simulating X-ray diffraction patterns produced from equilibrated MD trajectories. We tested systems built with 5 monomers per layer in the parallel displaced and sandwiched configurations. Simulated patterns were generated using portions of simulation trajectory after equilibration. The patterns for both structures are shown and compared to experiment in Figure 8.

Simulated XRD of the sandwiched configuration contains all experimental features except for R-helix. R-alkanes, R-spots and R-pores appear close to their expected locations. R- π is also present, however it intersects R-alkanes at a q_z value lower than experiment meaning the head groups in our model prefer to stack farther apart.

The parallel displaced configuration results in a simulated XRD pattern with the closest match to ex-

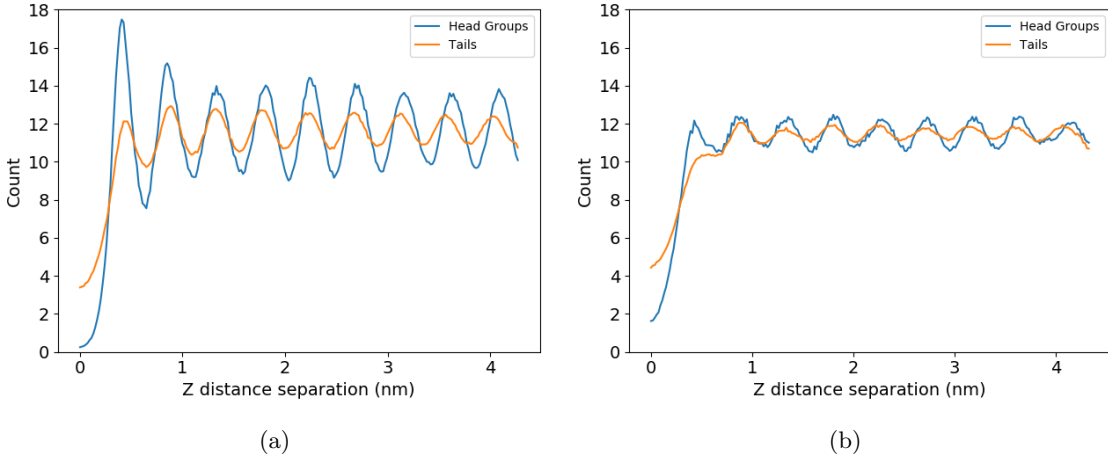


Figure 7: Pair distribution functions of aromatic carbons for the (a) 5 monomer per layer, sandwiched and (b) 5 monomer per layer, parallel displaced configurations. Clear periodic maxima in the z number density indicate distinct layers. The magnitude of the spikes with respect to the average suggest that the 5 monomer per layer, sandwiched configuration possesses a higher degree of layer partitioning.

periment. It produces the only pattern that exhibits all major reflections. R-alkanes and R-pores appear as they do in the sandwiched configuration. R-spots and R- π appears, however with a lower intensity relative to R-alkanes when compared to the sandwiched configuration. R-helix appears due to the parallel displaced aromatic rings. It is a subharmonic of R- π since the nearest vertically stacked head group to any given head group is 7.4 Å away.

In both the parallel displaced and sandwiched configurations, we noted that R- π appears in a location which corresponds to a real space separation larger than experiment. We attribute this discrepancy to GAFF's inability to appropriately model the aromatic interactions which would be necessary to achieve the correct π - π stacking distance. Systems have been modeled that exhibit the correct stacking distance, however they are typically made of planar molecules spanning a large area. The system we have modeled has bulky tails whose entropic contributions compete with the π - π stacking interaction energy. There have been efforts to model systems that contain π interactions in a classical mechanical context using polarizable forcefields. We could implement a polarizable force field, however it is likely not worth the extra computational cost. If our model proves to be inadequate when simulating transport, we will revisit our current choice of forcefield.

R-spots, which appears in both simulated XRD patterns, is a result of hexagonal alkane chain packing. Previously, the spots in the diffraction pattern had been explained as the product of tilted alkane chains. We measured the tilt angle of the alkane chains and showed that our system equilibrates to an average tilt angle close to zero degrees (Fig. 9). To understand the origin of the spots, we determined which atoms gave rise to the feature. Since R-spots is present as higher intensity spots within R-alkanes, it is likely that the spots arise as a consequence of the tails. By removing all non-tail atoms from the trajectory and simulating

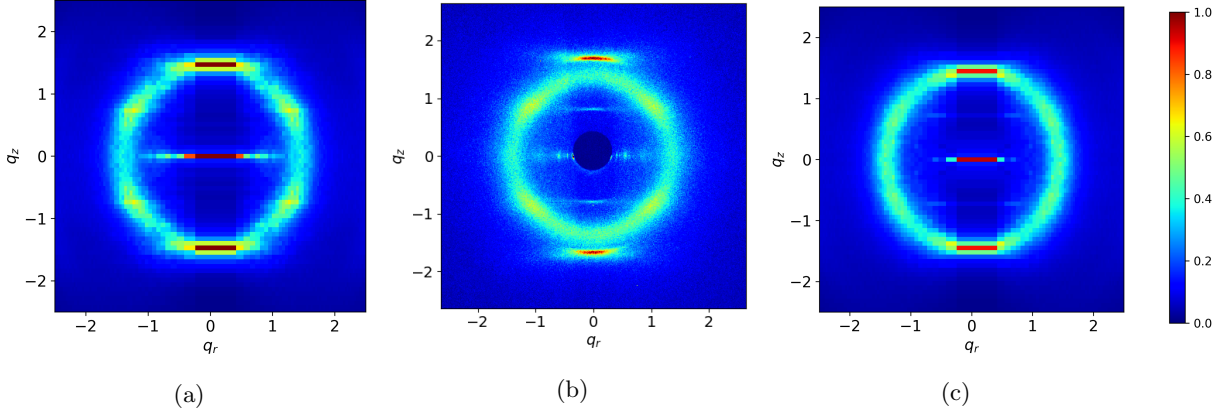


Figure 8: The simulated X-ray diffraction patterns for simulations run in the sandwiched (a) and parallel-displaced (c) configurations are compared to experiment (b). The parallel displaced configuration is the only one that exhibits all major reflections of interest to some degree

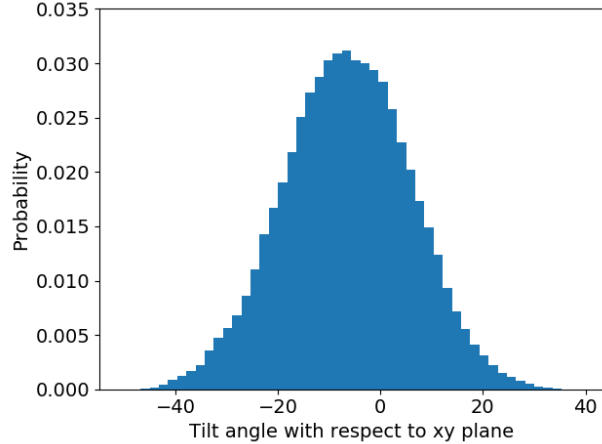


Figure 9: The tilt angle distribution of alkane chain tails with respect to the membrane plane indicates an average tilt angle near 7° which is far from the 37° tilt angle previously used to explain R-spots.

a diffraction pattern, we were able to isolate the cause of the spots to the tails (Figure 10). Since the tails stay nearly flat, we plotted the centroids of the tails and measured the angle between each centroid and its nearest neighbors with respect to the plane of the membrane. We see distinct peaks in the distribution of these angles (Figure 11).

The peaks in the nearest neighbor angle distribution are consistent with the location of R-spots. The peaks of interest in Figures 11a and 11c are located at $\pm 33^\circ$ which is the same location where the highest intensity of spots are located on the simulated patterns. We confirmed this conclusion by radially integrating the 2D WAXS pattern for $|\mathbf{q}|$ values between 1.4 and 1.57 (between 4 and 4.5 Å in real space). We observe that distinct peaks appear ca. 30° , in close agreement with the previously measured angle distribution

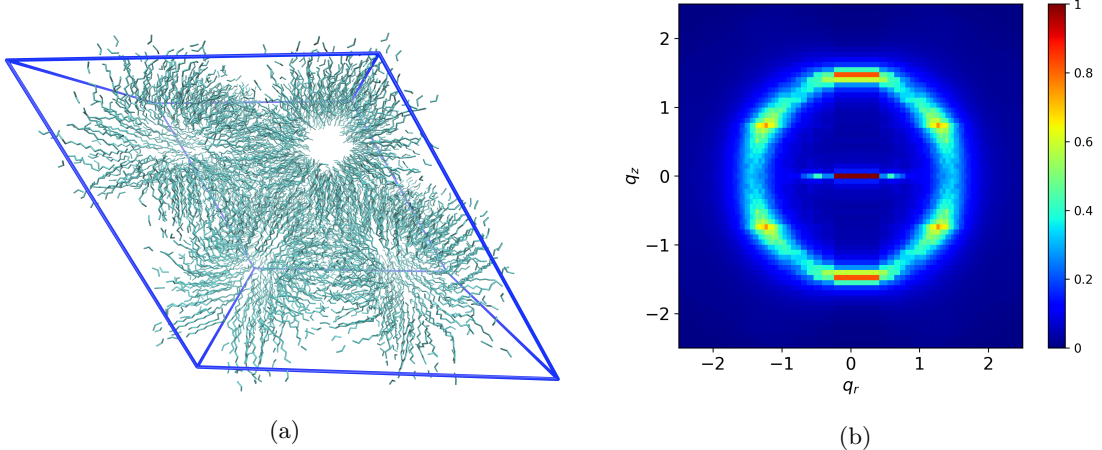


Figure 10: (a) All atoms except carbon atoms making up the tails are removed from a sandwiched configuration trajectory. (b) The simulated diffraction pattern of the tail-only trajectory still shows R-spots

(Figs. 11b and 11d). We performed the same integration on the raw experimental data and found the angle at which R-spots reaches its highest intensity to be $\pm 37^\circ$ which is a reconcilable difference with our simulated results.

3.2 Initial Layer Spacing Affects System Equilibration

When systems are built with layers stacked 5.0 Å apart then equilibrated, we observe long-term stability of a qualitatively different configuration suggesting that we have found another metastable free energy basin, further corroborating (4). We studied this type of system in both the parallel displaced and sandwiched configurations.

Structural properties are different when layers are initially spaced 5 Å apart. In both configurations, we observe a decrease in pore spacing (Fig. 12b) and a corresponding increase in the equilibrated distance between layers (Fig. 12a). The simulated X-ray diffraction patterns indicate further structural differences. In the parallel displaced configuration, almost all contrast between R-spots and R-alkanes is faded (Fig. 12c). In the sandwiched configuration, R-spots are weakly present, but in different locations, showing higher intensity at the top and bottom of the pattern as well as at the intersection of R-alkanes with $q_z = 0$ (Fig. 12d).

Neither assembly deviates from its initial head group arrangement. R-helix is still faintly visible in the parallel displaced configuration and is absent in the sandwiched simulated diffraction pattern. The spectroscopic signatures are unique to the two different head group configurations.

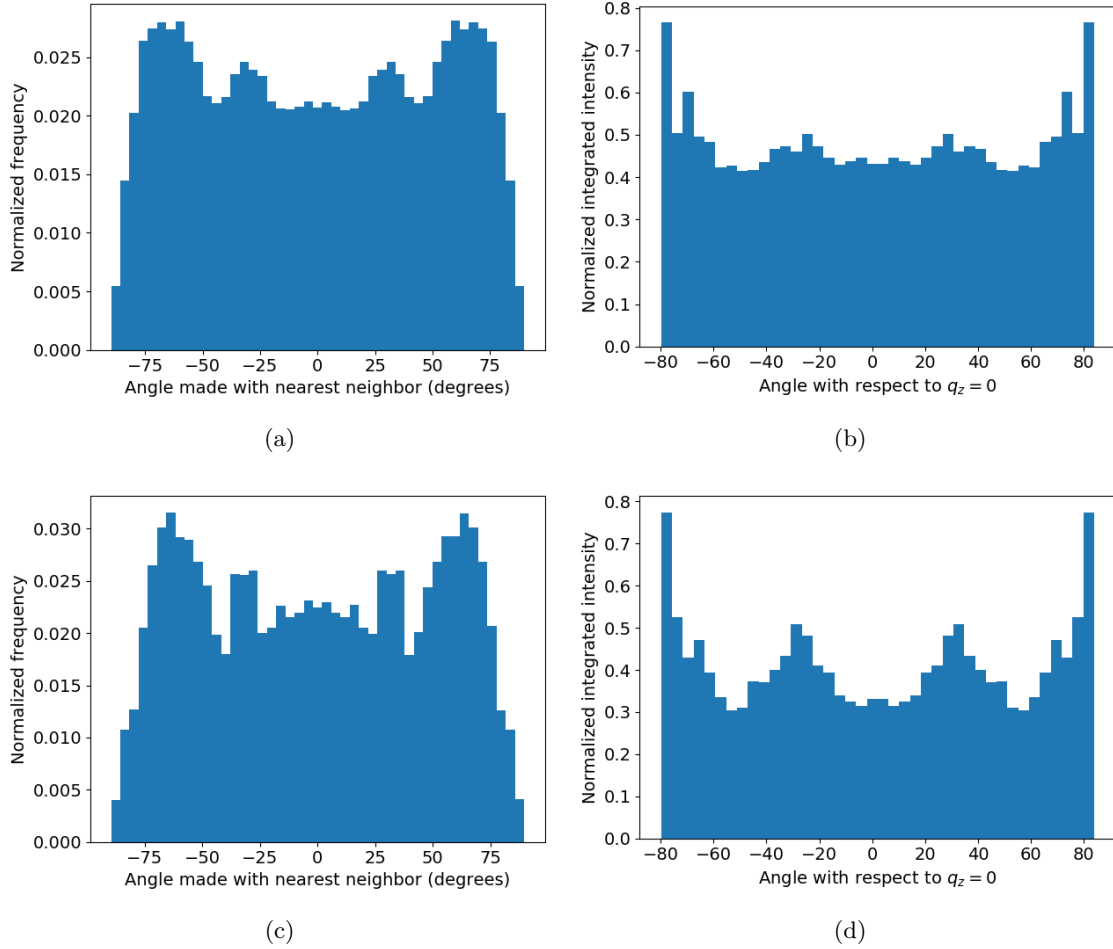


Figure 11: The distribution of angles w.r.t. the xy plane between alkane chain tail centroids and nearest neighbor centroids for equilibrated parallel displaced (a) and sandwiched (c) configurations. The same peaks are visible when the 2D simulated diffraction data is radially integrated in the R-alkanes region, (b) and (d) respectively.

3.3 Pore Structure Depends on Initial Configuration

In order to address (5), we plotted the number of densities of heavy atoms in the head group, carbon atoms in the tail region and the sodium ions (Figure 13). For the head group region, we used the carbon atoms making up the aromatic ring. For the tail region we used only carbon atoms of the monomer tails (See Supplemental Information for diagram). Histograms are averaged over at least 50 ns of equilibrated trajectory.

In all cases, the space in the pore region is filled with sodium ions and head groups. There is a clear partition between the hydrophobic and hydrophilic regions. Alkane tails do not cross into the pore region. We expect that when water is introduced to the system, water molecules will occupy the hydrophilic region and open up the pores for aqueous solute transport.

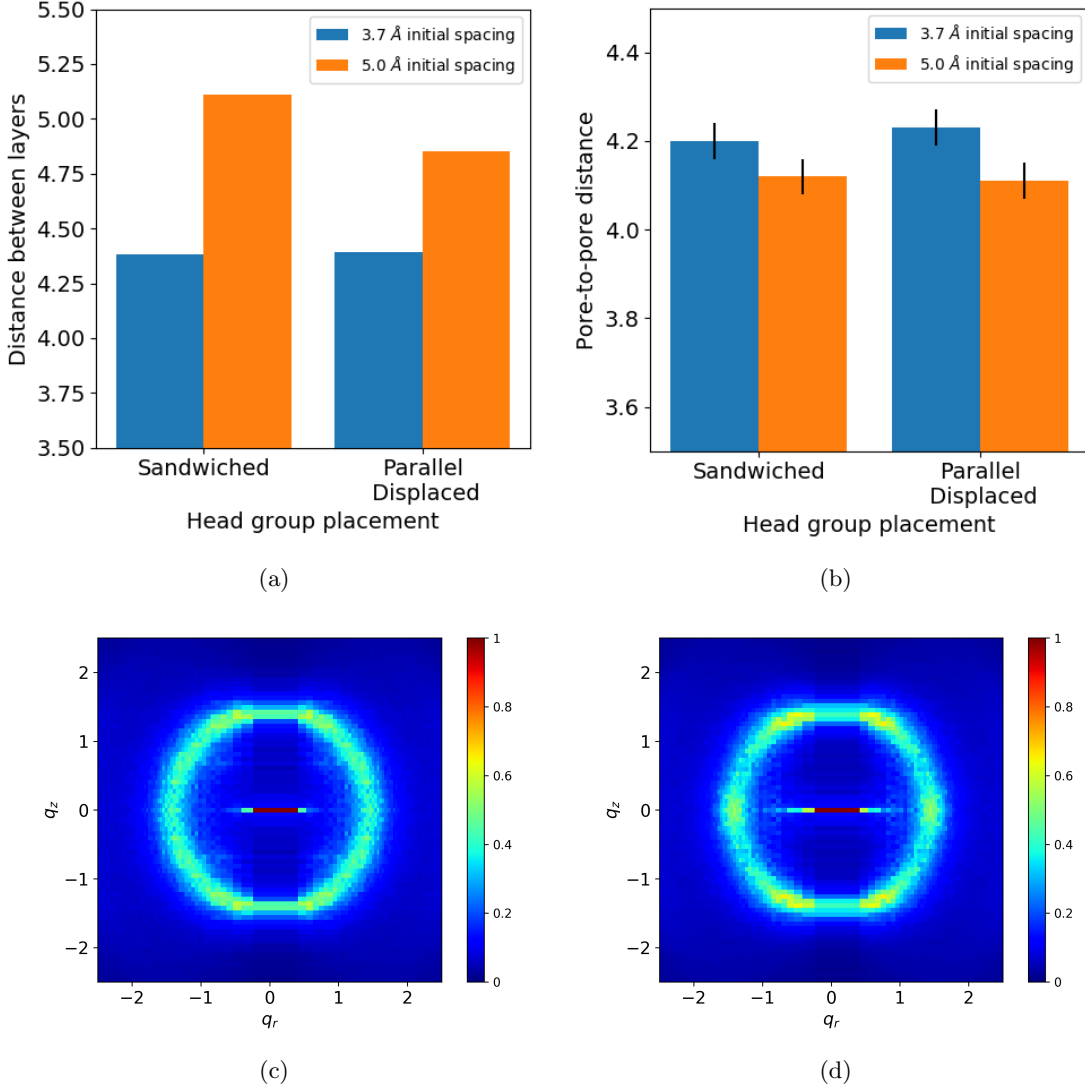


Figure 12: In comparison to systems built with 3.7 \AA initial layer spacing, the simulated X-ray diffraction patterns of the parrallel displaced (a) and sandwiched (b) configurations are different when systems are built with a 5 \AA initial layer spacing, most notably in the region bounded by R-alkanes. When layers are stacked further apart, the distance between layers increases (c) and the pore spacing decreases (d).

The sandwiched configuration (Fig. 13b) shows a relatively ordered pore structure. The number densities of components in all other configurations are comparable. In contrast, sodium ions and head groups in the sandwiched configuration are highly concentrated away from the pore center meaning that there is vacancy in the pore region. A vacant pore is very likely to be unstable in a real system, further supporting the physical realism of the parallel displaced configuration.

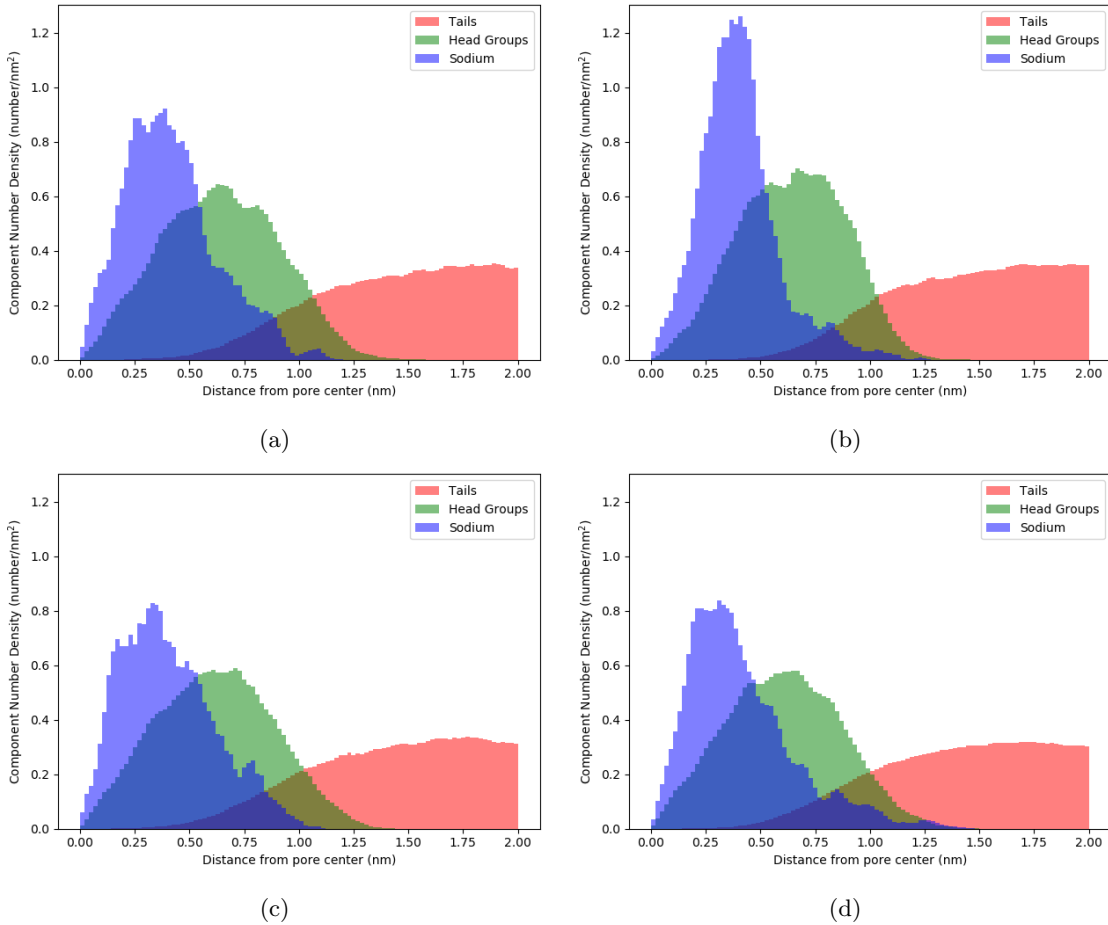


Figure 13: In all cases, assemblies stay partitioned into hydrophilic and hydrophobic regions. The parallel displaced (a), the disordered parallel displaced (c), and the disordered sandwiched (d) show similar pore structures. The sandwiched configuration (b) exhibits an open pore structure with sodium ions and head groups concentrated away from the pore center.

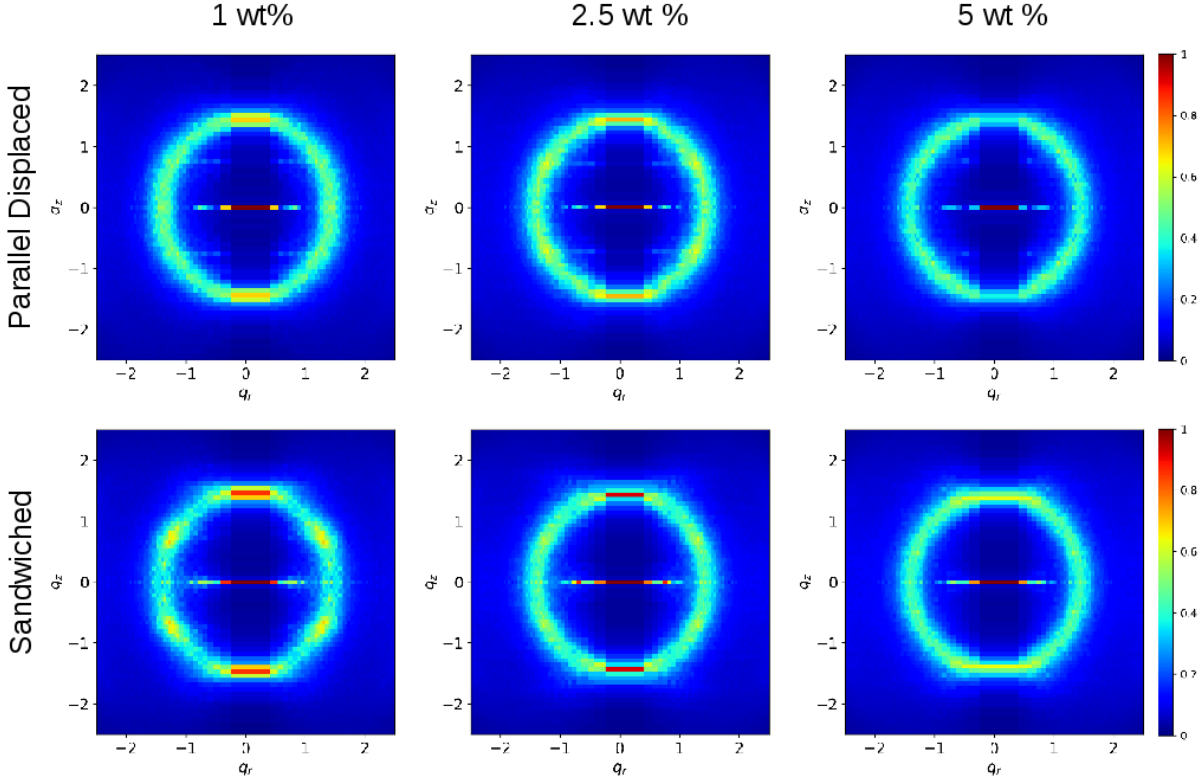


Figure 1: Simulated diffraction patterns generated from trajectories of systems built in the parallel displaced and sandwiched configurations as a function of water content shows weaker reflections than the dry system. All plots are scaled to use the same colorbar as their dry system counterpart

Figure 14

3.4 Affect of Water on Structure

We answered (6) and further support (3) by preparing parallel displaced and sandwiched configurations according to the wet equilibration procedure. There is no experimental measurement of trace water concentration in the pores so we tested a range of water concentrations from 0.5 to 5 percent. Our lower bound models a system with on average 2 water molecules for each monomer layer. Figure 14 shows the simulated diffraction patterns resulting from each configuration.

In all cases, water disrupts structuring of the model. The plots in Figure 14 are normalized to have the same colorbar as the dry systems. The intensity of the reflections decrease when water is added to the system. In systems built with 5 wt % water, R- π and R-spots become nearly indistinguishable from R-alkanes.

Water is not necessary to maintain an ordered pore structure. We do not eliminate the possibility that water is necessary in order to drive self-assembly, however, studying the mechanisms of self assembly is

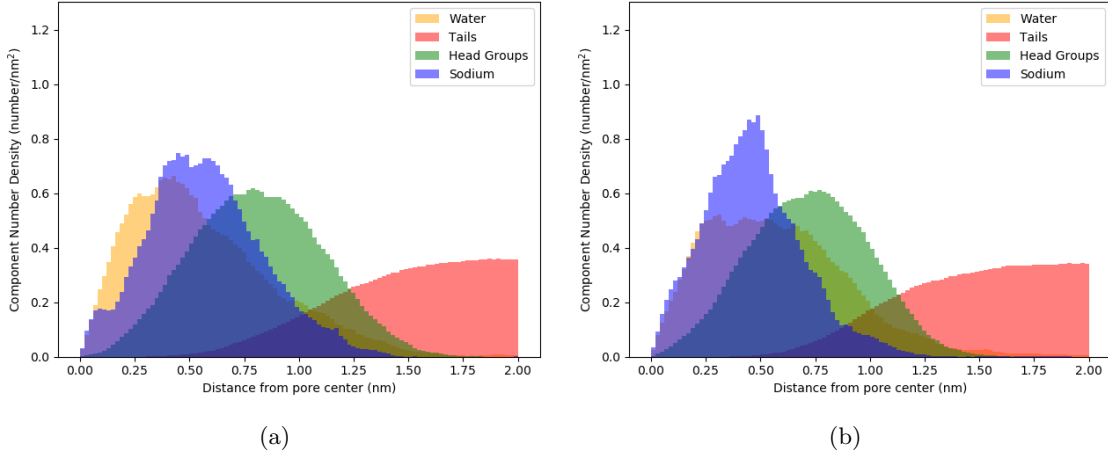


Figure 15: Water fills the membrane pores in the parallel displaced (a) and sandwiched (b) configurations. Sodium ions are distributed more uniformly in the sandwiched configuration.

beyond the scope of this work. According to our model, once the system has formed the Col_h phase, adding water only drives disorder of the pore structure. In the true equilibrium configuration, if water exists, it is primarily confined to the pore region where there is no driving force for aggregation of water molecules. In the case of trace water, water molecules will be too sparse to form a hydrogen bonding network.

In systems built with 5 wt % water, the pore region becomes filled with water. We plotted the number density of components in this system and see that the pores become a soup of water molecules and sodium ions (Fig. 15). This system is a closer representation of the H_{II} phase which is typically synthesized with ca. 8 wt % water. We believe that the hydrated membrane pores will be valuable for aqueous separations. Further analysis of and transport within the H_{II} phase are left for future studies.

3.5 Model Ionic Conductivity Measurements

We used the equilibrated parallel displaced system to calculate ionic conductivity since its structure is the closest match to experiment. The model gives reasonable estimates of ionic conductivity when compared to experiment. Calculated values of ionic conductivity obtained using the Nernst-Einstein relation and Collective Diffusion model are compared in Figure 16. The two methods agree with each other within error, although the uncertainty obtained using the Collective Diffusion model is much higher. Much longer simulations are needed to lower the uncertainty, however it is not feasible to do so with a large system. We will only use the Nernst-Einstein relation in future calculations of this type.

The calculated values of ionic conductivity are higher than experiment by an order of magnitude. One can justify the reason for this result by considering the real system studied experimentally. The ionic conductivity measurement to which we are comparing was done on a 80 μm thick film, nearly 10,000 times thicker than our

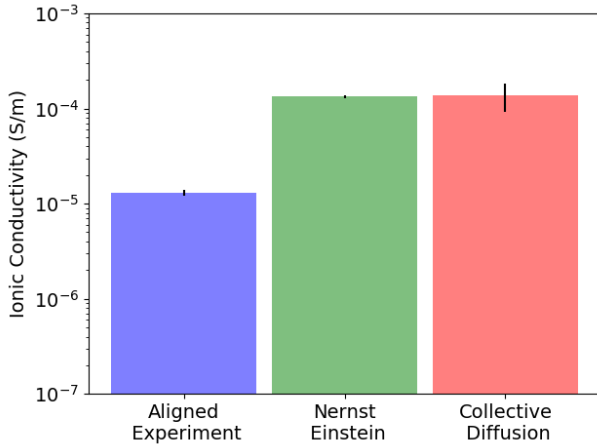


Figure 16: Calculated ionic conductivity using the Nernst-Einstein relation and Collective Diffusion model agree with error. Both methods give calculated values of ionic conductivity an order of magnitude higher than the experimental value.

simulated system. The thick film likely has defects leading to non-contiguous pores and imperfect alignment. It has been shown that there is a large dependence of ionic conductivity on the alignment of the pores. The ionic conductivity of an unaligned film is ca. 85 times lower than that of a nearly aligned film referenced here. We hypothesize that a thin, perfectly aligned film would have a value of ionic conductivity in close agreement with our model.

3.6 Affect of Crosslinking

The system's structure and physical characteristics did not change significantly when we applied the crosslinking algorithm to the equilibrated parallel-displaced configuration built with 5 monomers per layer. We simulated the crosslinked system in the NPT ensemble for 100 ns. The distance between pores shrinks by 0.4 Å and the distance between layers increases by 0.04 Å after the system is crosslinked. All major features are still present in the simulated XRD patterns, however at lower intensities (Fig. 17a). We calculated the ionic conductivity using the Nernst-Einstein relation and found that it is lower in the crosslinked system (Fig. 17b).

4 Conclusion

We have used a detailed molecular model of the Col_h phase formed by Na-GA3C11 in order to study its nanoscopic structure. While there have been efforts to model formation of various liquid crystalline phases with molecular dynamics, to our knowledge there have been no studies which attempt to examine their structure with the same level of detail presented here. Evidence strongly supports that monomers stay

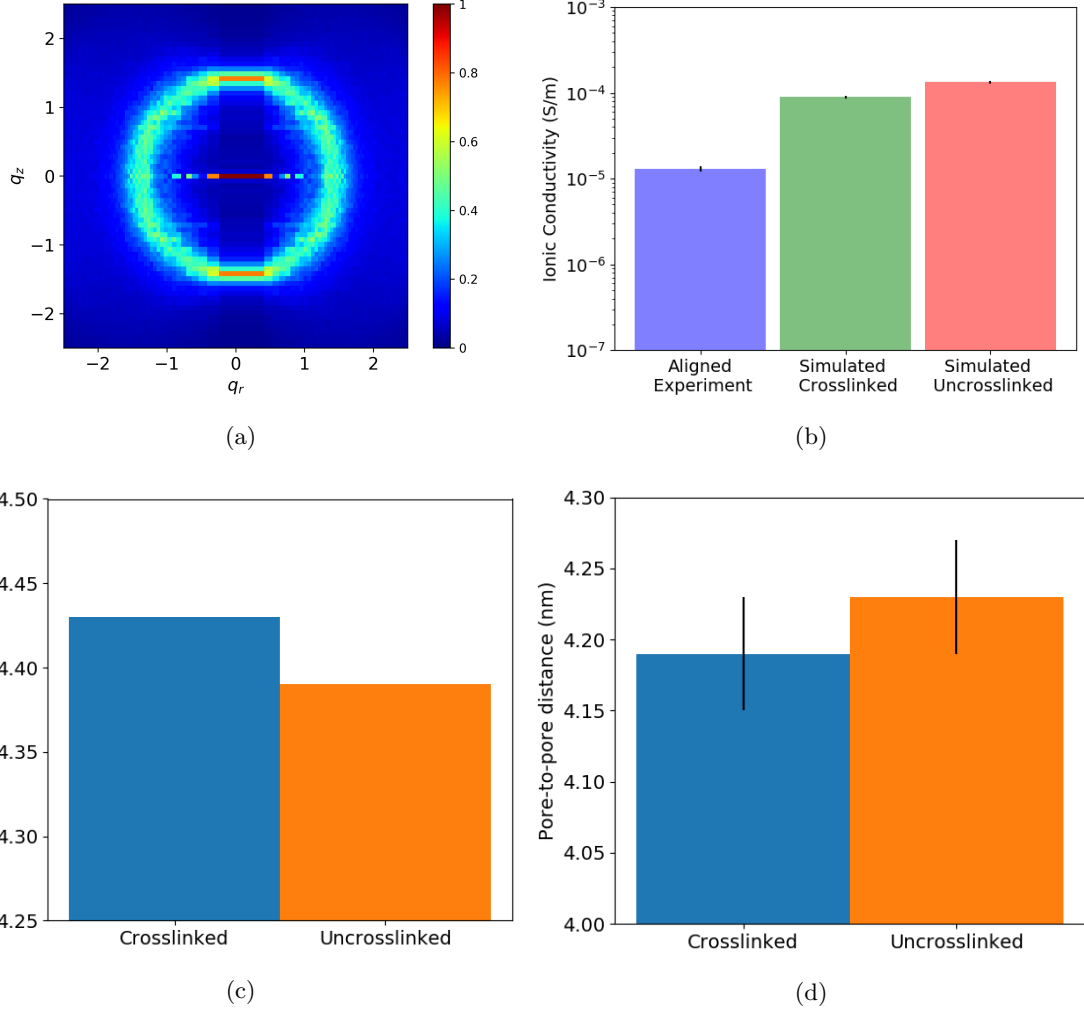


Figure 17: (a) Reflections produced by the crosslinked configuration fade relative to the uncrosslinked system. The colorbar shown is the same used for the uncrosslinked system. (b) The ionic conductivity is smaller relative to the uncrosslinked system, but still much larger than the experimental value. (c) The distance between layers increases when the system is crosslinked. (d) The pore spacing decreases when the membrane is crosslinked.

partitioned into layers and that each layer contains 5 monomers. We have explored the affect of two different π - π stacking modes on the equilibrated membrane strucure. Simulated diffraction patterns generated from MD trajectories suggest that the parallel-displaced configuration produces a structure with the closest match to experiment. Finally, water is not needed to create well-defined pore structures.

Now that we have a good idea of what the membrane structure should look like, we will evaluate transport of various solutes within the system. We will apply the knowledge gained from this study in order to suggest improvements to the existing system as well as to evaluate new unsynthesized LLC systems.

References

- [1] T. Humplik, J. Lee, S. C. OHern, B. A. Fellman, M. A. Baig, S. F. Hassan, M. A. Atieh, F. Rahman, T. Laoui, R. Karnik, and E. N. Wang, “Nanostructured materials for water desalination,” *Nanotechnology*, vol. 22, no. 29, p. 292001, 2011.
- [2] B. Van Der Bruggen, C. Vandecasteele, T. Van Gestel, W. Doyen, and R. Leysen, “A review of pressure-driven membrane processes in wastewater treatment and drinking water production,” *Environmental Progress*, vol. 22, pp. 46–56, Apr. 2003.
- [3] J. G. Wijmans and R. W. Baker, “The solution-diffusion model: a review,” *Journal of Membrane Science*, vol. 107, pp. 1–21, Nov. 1995.
- [4] C. Fritzmann, J. Lwenberg, T. Wintgens, and T. Melin, “State-of-the-art of reverse osmosis desalination,” *Desalination*, vol. 216, pp. 1–76, Oct. 2007.
- [5] W. R. Bowen and J. S. Welfoot, “Modelling the performance of membrane nanofiltrationcritical assessment and model development,” *Chemical Engineering Science*, vol. 57, pp. 1121–1137, Apr. 2002.
- [6] D. Cohen-Tanugi, L.-C. Lin, and J. Grossman, “Multilayer Nanoporous Graphene Membranes for Water Desalination,” *Nano Letters*, vol. 16, pp. 1027–1033, Jan. 2016.
- [7] K. Hata, D. N. Futaba, K. Mizuno, T. Namai, M. Yumura, and S. Iijima, “Water-Assisted Highly Efficient Synthesis of Impurity-Free Single-Walled Carbon Nanotubes,” *Science*, vol. 306, pp. 1362–1364, Nov. 2004.
- [8] S. Maruyama, E. Einarsson, Y. Murakami, and T. Edamura, “Growth process of vertically aligned single-walled carbon nanotubes,” *Chemical Physics Letters*, vol. 403, pp. 320–323, Feb. 2005.
- [9] S. MURAD, K. ODER, and J. LIN, “Molecular simulation of osmosis, reverse osmosis, and electroosmosis in aqueous and methanolic electrolyte solutions,” *Molecular Physics*, vol. 95, pp. 401–408, Oct. 1998.
- [10] L. Li, J. Dong, T. M. Nenoff, and R. Lee, “Desalination by reverse osmosis using MFI zeolite membranes,” *Journal of Membrane Science*, vol. 243, pp. 401–404, Nov. 2004.
- [11] X. Feng, M. E. Tousley, M. G. Cowan, B. R. Wiesnauer, S. Nejati, Y. Choo, R. D. Noble, M. Elimelech, D. L. Gin, and C. O. Osuji, “Scalable Fabrication of Polymer Membranes with Vertically Aligned 1 nm Pores by Magnetic Field Directed Self-Assembly,” *ACS Nano*, vol. 8, pp. 11977–11986, Dec. 2014.

- [12] R. C. Smith, W. M. Fischer, and D. L. Gin, “Ordered Poly(p-phenylenevinylene) Matrix Nanocomposites via Lyotropic Liquid-Crystalline Monomers,” *Journal of the American Chemical Society*, vol. 119, no. 17, pp. 4092–4093, 1997.
- [13] M. Zhou, T. J. Kidd, R. D. Noble, and D. L. Gin, “Supported Lyotropic Liquid-Crystal Polymer Membranes: Promising Materials for Molecular-Size-Selective Aqueous Nanofiltration,” *Advanced Materials*, vol. 17, pp. 1850–1853, Aug. 2005.
- [14] R. Resel, U. Theissl, C. Gadermaier, E. Zojer, M. Kriechbaum, H. Amenitsch, D. Gin, R. Smith, and G. Leising, “The H₂-phase of the lyotropic liquid crystal sodium 3,4,5-tris(omega-acryloyloxyundecyloxy)benzoate,” *Liquid Crystals*, vol. 27, pp. 407–411, Mar. 2000.
- [15] X. Feng, S. Nejati, M. G. Cowan, M. E. Tousley, B. R. Wiesnauer, R. D. Noble, M. Elimelech, D. L. Gin, and C. O. Osuji, “Thin Polymer Films with Continuous Vertically Aligned 1 nm Pores Fabricated by Soft Confinement,” *ACS Nano*, vol. 10, pp. 150–158, Jan. 2016.
- [16] R. Resel, G. Leising, P. Markart, M. Kriechbaum, R. Smith, and D. Gin, “Structural properties of polymerised lyotropic liquid crystals phases of 3,4,5-tris(\$mega\$-acryloxyalkoxy)benzoate salts,” *Macromolecular Chemistry and Physics*, vol. 201, no. 11, pp. 1128–1133, 2000.
- [17] E. S. Hatakeyama, C. J. Gabriel, B. R. Wiesnauer, J. L. Lohr, M. Zhou, R. D. Noble, and D. L. Gin, “Water filtration performance of a lyotropic liquid crystal polymer membrane with uniform, sub-1-nm pores,” *Journal of Membrane Science*, vol. 366, no. 1-2, pp. 62–72, 2011.
- [18] X. Zhu, M. Scherbina, A. Bakirov, B. Gorzolnik, S. Chvalun, U. Beginn, and M. Moller, “Methacrylated Self-Organizing 2,3,4-Tris(alkoxy)benzenesulfonate: A New Concept Toward Ion-Selective Membranes,” *ACS: Chemistry of Materials*, vol. 18, no. 19, pp. 4667–4673, 2006.
- [19] E. Gazit, “A possible role for -stacking in the self-assembly of amyloid fibrils,” *The FASEB Journal*, vol. 16, pp. 77–83, Jan. 2002.
- [20] M. O. Sinnokrot, E. F. Valeev, and C. D. Sherrill, “Estimates of the Ab Initio Limit for Interactions: The Benzene Dimer,” *Journal of the American Chemical Society*, vol. 124, pp. 10887–10893, Sept. 2002.
- [21] M. P. Waller, A. Robertazzi, J. A. Platts, D. E. Hibbs, and P. A. Williams, “Hybrid density functional theory for -stacking interactions: Application to benzenes, pyridines, and DNA bases,” *Journal of Computational Chemistry*, vol. 27, pp. 491–504, Mar. 2006.

- [22] A. L. Ringer, M. O. Sinnokrot, R. P. Lively, and C. D. Sherrill, “The Effect of Multiple Substituents on Sandwich and T-Shaped Interactions,” *Chemistry A European Journal*, vol. 12, pp. 3821–3828, May 2006.
- [23] J. Wang, R. M. Wolf, J. W. Caldwell, P. A. Kollman, and D. A. Case, “Development and testing of a general amber force field,” *Journal of Computational Chemistry*, vol. 25, pp. 1157–1174, July 2004.
- [24] J. Wang, W. Wang, P. A. Kollman, and D. A. Case, “Automatic atom type and bond type perception in molecular mechanical calculations,” *Journal of Molecular Graphics and Modelling*, vol. 25, pp. 247–260, Oct. 2006.
- [25] D. Case, R. Betz, W. Botello-Smith, D. Cerutti, T. Cheatham, III, T. Darden, R. Duke, T. Giese, H. Gohlke, A. Goetz, N. Homeyer, S. Izadi, P. Janowski, J. Kaus, A. Kovalenko, T. Lee, S. LeGrand, P. Li, C. Lin, T. Luchko, R. Luo, B. Madej, D. Mermelstein, K. Merz, G. Monard, H. Nguyen, H. Nguyen, I. Omelyan, A. Onufriev, D. Roe, A. Roitberg, C. Sagui, C. Simmerling, J. Swails, R. Walker, J. Wang, R. Wolf, X. Wu, L. Xiao, D. York, and P. Kollman, “AmberTools16,” Apr. 2016.
- [26] H. Bekker, H. J. C. Berendsen, E. J. Dijkstra, S. Achterop, R. van Drunen, D. van der Spoel, A. Si-jbers, H. Keegstra, B. Reitsma, and M. K. R. Renardus, “Gromacs: A parallel computer for molecular dynamics simulations,” *Physics Computing*, 1993.
- [27] H. J. C. Berendsen, D. van der Spoel, and R. van Drunen, “GROMACS: A message-passing parallel molecular dynamics implementation,” *Computer Physics Communications*, vol. 91, pp. 43–56, Sept. 1995.
- [28] D. Van Der Spoel, E. Lindahl, B. Hess, G. Groenhof, A. E. Mark, and H. J. C. Berendsen, “GROMACS: Fast, flexible, and free,” *Journal of Computational Chemistry*, vol. 26, pp. 1701–1718, Dec. 2005.
- [29] B. Hess, C. Kutzner, D. van der Spoel, and E. Lindahl, “GROMACS 4: Algorithms for Highly Efficient, Load-Balanced, and Scalable Molecular Simulation,” *Journal of Chemical Theory and Computation*, vol. 4, pp. 435–447, Mar. 2008.
- [30] J. Mondal, M. Mahanthappa, and A. Yethiraj, “Self-Assembly of Gemini Surfactants: A Computer Simulation Study,” *The Journal of Physical Chemistry B*, vol. 117, pp. 4254–4262, Apr. 2013.
- [31] L. Martnez, R. Andrade, E. G. Birgin, and J. M. Martnez, “PACKMOL: A package for building initial configurations for molecular dynamics simulations,” *Journal of Computational Chemistry*, vol. 30, pp. 2157–2164, Oct. 2009.

- [32] A. Einstein, “Investigations on the theory of the brownian movement,” *Dover Publications*, 1956.
- [33] Y. Liu and F. Zhu, “Collective diffusion model for ion conduction through microscopic channels,” *Biophysical Journal*, vol. 104, pp. 368–376, Jan. 2013.